

Advanced technique for assessment of spatially averaged dosimetric quantities on non-planar surfaces

Proposal of the dissertation topic

Ante Kapetanović

Faculty of Electrical Engineering, Mechanical Engineering and Naval Architecture (FESB)

April 24, 2023



Jury Members

President: prof Zoran Blažević, PhD

Examiners: prof Zvonimir Šipuš, PhD Supervisor: prof Dragan Poljak, PhD
 assoc prof Vicko Dorić, PhD
 assoc prof Mario Cvetković, PhD

Table of contents

1. Introduction

Problem and object of scientific research

Related work

Motivation, purpose and objectives of the research

Hypothesis

2. Materials and methods

Non-planar models

Normal estimation

Surface integration

“Hot-spot” detection

3. Applications and experimental results

4. Concluding remarks

Table of contents

- 1. Introduction**
- 2. Materials and methods**
- 3. Applications and experimental results**
- 4. Concluding remarks**

Problem and object of scientific research

- the rise of data-intensive wireless devices → expansion of the utilized radio frequency (RF) spectrum into millimeter waves (MMW)¹
- global roll-out of the fifth-generation (5G) standard for broadband cellular networks → improved communication performance by increasing channel capacity and reducing network latency through²:
 - carrier aggregation
 - multiple-input multiple-output (MIMO) technology
 - beam-forming (or spatial filtering)
 - frequency range (FR 1 (0.45–6 GHz), FR 2 (24.25–52.6 GHz))
- a growing public concern about adverse health effects from exposure to RF electromagnetic (EM) radiation³
- to ensure absolute safety, various international bodies prescribe *exposure limits* derived upon relevant scientific literature

¹Rappaport et al. 2013.

²Andrews et al. 2014.

³Wu, Rappaport, and Collins 2015.

But what is EM radiation?

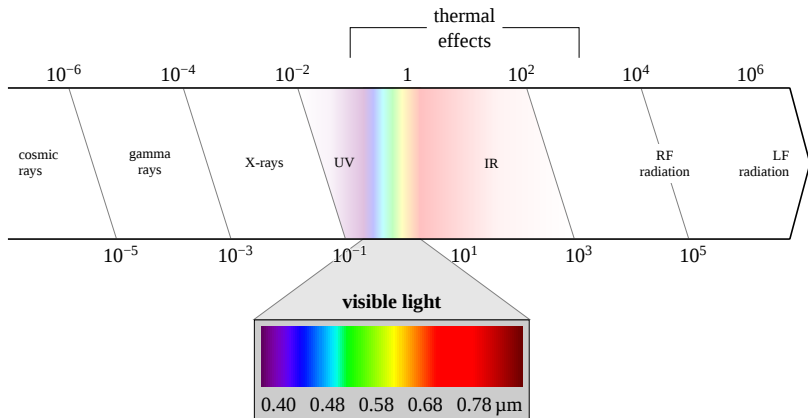


Figure: Diagram of the EM spectrum as a function of wavelength. *Ionizing radiation* occurs when a photon's energy is greater than 10 eV – below the lower end of ultraviolet (UV) spectrum. Visible light, infrared (IR), RF and low-frequency (LF) radiation is thus considered *non-ionizing*.

Non-ionizing EM radiation effects on biological tissue

⁴International Commission on Non-Ionizing Radiation Protection (ICNIRP) 2020b.

⁵World Health Organization (WHO) 2022.

⁶Ziskin et al. 2018.

Exposure limits to artificial EM fields

- prescribed by internationally recognized guidelines⁷ and standards⁸
- protection against adverse health effects by respecting the frequency- and exposure scenario-dependent limits
- reduction factors applied in a conservative manner (inter-individual variability, uncertainties related to exposure setup or environment, etc.)
- threshold values → *basic restrictions* or (BR) → *reference levels* (RL)
 - whole-body or localized exposure
 - brief or steady-state exposure
- the *specific absorption rate* (SAR) used as BR for the steady-state core (whole-body average) and localized (10-g average) temperature rise from 100 kHz to 300 GHz
- the *incident power density* in free space used as RL to provide practical means of demonstrating compliance

⁷International Commission on Non-Ionizing Radiation Protection (ICNIRP) 2020a.

⁸IEEE International Committee on Electromagnetic Safety (ICES) Technical Committee (TC) 95 2019.

Exposure assessment and dosimetry in era of 5G

- at 6 GHz, 90 % of the power is absorbed within the uppermost layer of the exposed tissue
- BR set in terms of the area-averaged *absorbed power density* (APD)
- line integral of SAR depth-wise into the tissue → *transmitted power density* (TPD)
- area-averaged TPD ≡ area-averaged APD → consistency and continuity with volume-averaged SAR

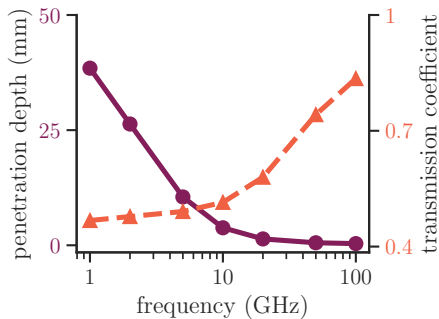


Figure: Penetration depth and transmission coefficient as a function of frequency.

Exposure assessment and dosimetry in era of 5G

- at 6 GHz, 90 % of the power is absorbed within the uppermost layer of the exposed tissue
- BR set in terms of the area-averaged *absorbed power density* (APD)
- line integral of SAR depth-wise into the tissue → *transmitted power density* (TPD)
- area-averaged TPD ≡ area-averaged APD → consistency and continuity with volume-averaged SAR

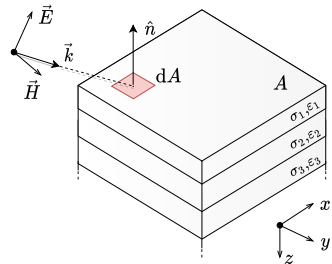


Figure: Averaging area on the exposed tissue surface from 3-D point of view.

Exposure assessment and dosimetry in era of 5G

- at 6 GHz, 90 % of the power is absorbed within the uppermost layer of the exposed tissue
- BR set in terms of the area-averaged *absorbed power density* (APD)
- line integral of SAR depth-wise into the tissue → *transmitted power density* (TPD)
- area-averaged TPD ≡ area-averaged APD → consistency and continuity with volume-averaged SAR

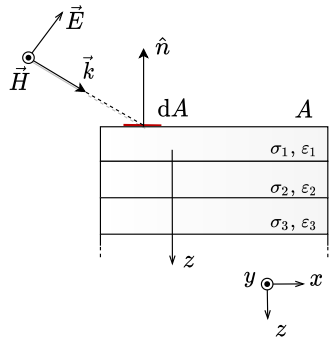


Figure: Averaging area on the exposed tissue surface from the lateral point of view.

Exposure assessment and dosimetry in era of 5G

- at 6 GHz, 90 % of the power is absorbed within the uppermost layer of the exposed tissue
- BR set in terms of the area-averaged *absorbed power density* (APD)
- line integral of SAR depth-wise into the tissue → *transmitted power density* (TPD)
- area-averaged TPD ≡ area-averaged APD → consistency and continuity with volume-averaged SAR

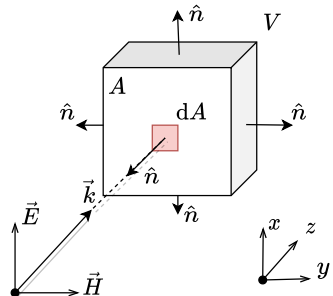


Figure: A cube of tissue for the volumetric averaging of SAR during localized steady-state exposure.

Mathematical definition of APD

- recent major revisions of IEEE/ICES standard (in 2019) and ICNIRP guidelines (in 2020) have identified two definitions of the spatially averaged APD:
 - ➊ area-averaged power density flux
 - ➋ area-averaged TPD

$$sPD_{ab,1} = \frac{1}{2A} \iint_A \Re[\mathbf{E} \times \mathbf{H}^*] \hat{\mathbf{n}} \, dA$$

- \mathbf{E}, \mathbf{H} – peak values of the complex phasor electric and magnetic field on the surface
- A – frequency-dependent averaging area
- $\hat{\mathbf{n}}$ – unit normal vector on A
- dA – integral area element

Mathematical definition of APD

- recent major revisions of IEEE/ICES standard (in 2019) and ICNIRP guidelines (in 2020) have identified two definitions of the spatially averaged APD:

- ① area-averaged power density flux
- ② area-averaged TPD

$$sPD_{ab,2} = \frac{1}{A} \iint_A \int_z \rho \text{ SAR } dz \, dA$$

where

$$\text{SAR} = \frac{\sigma |E|^2}{2\rho}$$

- E – peak value of the complex phasor electric field within tissue
- σ – conductivity of tissue
- ρ – tissue density

Mathematical definition of IPD

- IPD is defined as the modulus of the time-averaged Poynting vector assuming free space conditions

$$S_{\text{inc}} = |\mathbf{E} \times \mathbf{H}^*|$$

- multiple definitions of the spatially averaged IPD have been proposed and discussed⁹ with two standing out in particular:

- the normal component of the time-averaged Poynting vector

$$sPD_{\text{inc, n}} = \frac{1}{2A} \iint_A \Re[\mathbf{E} \times \mathbf{H}^*] \cdot \hat{\mathbf{n}} \, dA$$

- the magnitude of the time-averaged Poynting vector

$$sPD_{\text{inc, tot}} = \frac{1}{2A} \iint_A |\mathbf{E} \times \mathbf{H}^*| \, dA$$

⁹IEEE International Committee on Electromagnetic Safety (ICES) Technical Committee (TC) 95 2021.

Practical considerations for the averaging area

- 2–6 GHz → peak value of the power density
- ≥ 6 GHz → averaging on 4 cm^2 square evaluation plane¹⁰
- ≥ 30 GHz → averaging on 1 cm^2 square evaluation plane in addition to account for narrow beam formation¹¹
- the power density spatially averaged on 1 cm^2 area should not exceed twice the value of the 4 cm^2 area¹²

¹⁰Funahashi, Ito, et al. 2018; Hashimoto et al. 2017.

¹¹Foster, Ziskin, and Balzano 2016.

¹²International Commission on Non-Ionizing Radiation Protection (ICNIRP) 2020a.

Tissue models and averaging area

- above 6 GHz, planar tissue-equivalent single- or three/four-layer models commonly utilized¹³:
 - stratum corneum
 - viable epidermis and dermis
 - hypodermis
 - muscle
- dielectric properties ← four-term Cole-Cole model¹⁴
- the construction of the averaging area on a planar evaluation surface – IEC/IEEE 63195-2:2022 international standard

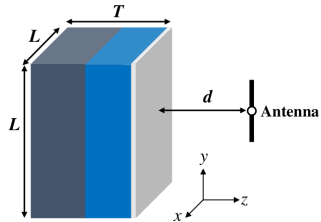


Figure: Skin models with different tissue compositions and the exposure condition. Taken from the recent international inter-comparison study by Li et al. 2021.

¹³Zhadobov et al. 2011.

¹⁴Gabriel 1996.

Current state of the research: a short synthesis

- from SAR to IPD, transition frequency of 6 GHz¹⁵
- harmonization of the area of an evaluation surface between guidelines and standards¹⁶
- 4 cm² and 1 cm² square averaging area on a planar evaluation surface¹⁷
- the first mention of the spatially averaged TPD as a potential BR above 6 GHz¹⁸
- validity of the IPD¹⁹ – correlation with the resultant surface temperature rise under various exposure conditions and different skin and antenna models is satisfactory (Pearson coefficient > 0.7 , $p < 0.05$)²⁰
- validity of the APD²¹ – by using the heating factor²²

¹⁵Anderson, Croft, and McIntosh 2010; McIntosh and Anderson 2010.

¹⁶Colombi, Thors, and Törnevik 2015; Thors et al. 2016; Xu et al. 2017.

¹⁷Foster, Ziskin, and Balzano 2016, 2017; Funahashi, Ito, et al. 2018; Hashimoto et al. 2017.

¹⁸Funahashi, Hirata, et al. 2018.

¹⁹Carrasco et al. 2019; Diao, K. Li, et al. 2021; He et al. 2018; K. Li, Sasaki, Watanabe, et al. 2019; Miura et al. 2021; Morimoto and Hirata 2022; Nakae et al. 2020; Sasaki et al. 2017.

²⁰De Santis et al. 2022.

²¹K. Li, Kodera, et al. 2023; K. Li, Sasaki, Wake, et al. 2021; Taguchi et al. 2022.

²²Foster, Ziskin, Balzano, and Bit-Babik 2018.

Beyond the state of the art

- non-planar body parts, e.g., fingers²³, ears²⁴, with the curvature radius \sim wavelength of the incident EM field
→ underestimation of the area-averaged quantities
- non-planar tissue models currently discussed within IEEE ICES TC95 SC6 WG7
 - canonical shapes, e.g., sphere or cylinder²⁵
 - anatomical tissue models²⁶

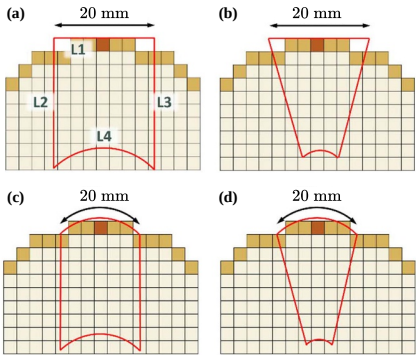


Figure: Reference averaging volumes/areas for different APD computation schemes. Taken from the study by Diao, Rashed and Hirata 2020.

²³C.-H. Li et al. 2012.

²⁴Sacco, Haider, and Zhadobov 2022.

²⁵Diao, Rashed, and Hirata 2020; Kapetanovic and Poljak 2022.

²⁶Kapetanovic, Sacco, et al. 2022.

Motivation, purpose and objectives of the research

- to quantitatively and qualitatively *investigate the influence of tissue surface morphology* on the values of extracted APD and IPD values above 6 GHz
- to develop an *accurate numerical integrator* for spatial averaging of power flow regardless of the numerical/analytical technique used in EM field calculations
- to develop a *computationally efficient automatic detection of the worst case scenario* – the “hot-spot” region – on the exposed surface of arbitrarily shaped tissue

Hypothesis

- ① traditional flat surfaces for the spatial averaging of the power density is inadequate for RF EM fields with wavelengths comparable to the approximate curvature radius of the non-planar body parts exposed

Assumption 1

cylindrical or spherical models are better suited for practical compliance assessment for exposure of common non-planar body parts, e.g., fingers, outer ear, head

Assumption 2

the distribution of normal vectors significantly affects the absorption of the incident EM field

Assumption 3

hybridization of machine learning and traditional numerical methods can effectively detect worst-case exposure scenario

Hypothesis

- ② anatomical models with irregularities and asymmetries characterized by intricate convex-concave tissue structures on the surface require the high fidelity numerical estimation of unit vectors normal on the surface

Assumption 1

cylindrical or spherical models are better suited for practical compliance assessment for exposure of common non-planar body parts, e.g., fingers, outer ear, head

Assumption 2

the distribution of normal vectors significantly affects the absorption of the incident EM field

Assumption 3

hybridization of machine learning and traditional numerical methods can effectively detect worst-case exposure scenario

Hypothesis

- ③ heterogeneous EM absorption in the near field require evaluating the spatially averaged power density over the entire exposed surface

Assumption 1

cylindrical or spherical models are better suited for practical compliance assessment for exposure of common non-planar body parts, e.g., fingers, outer ear, head

Assumption 2

the distribution of normal vectors significantly affects the absorption of the incident EM field

Assumption 3

hybridization of machine learning and traditional numerical methods can effectively detect worst-case exposure scenario

Table of contents

1. Introduction

2. Materials and methods

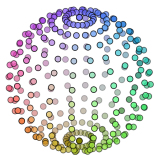
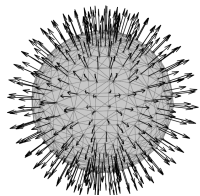
3. Applications and experimental results

4. Concluding remarks

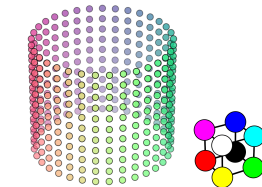
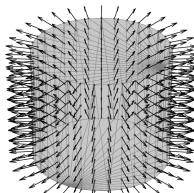
Overview

- development of the averaging method of IPD/APD on curved surface of canonical non-planar models – currently discussed within IEEE/ICES TC95 SC6 working group 7
- anatomical models – averaging highly dependent on the underlying numerical method of the software used for the exposure scenario simulation
- estimation of surface normals – crucial for computing the flux in definitions of both the spatially averaged IPD and APD
- propagation-direction power density into the evaluation surface – contributions from regions where the Poynting vector is oriented *outward* from the evaluation surface or for regions of the surface *close to parallel* to the direction of the Poynting vector should be avoided
- effective, fast and plausible procedure to detect the “hot-spot” region which yields the maximum spatially averaged power density

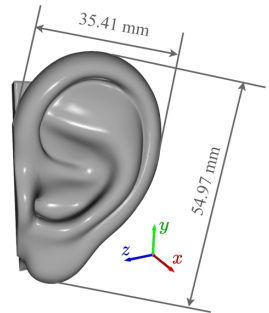
Non-planar models



(a) Spherical model with radius set to 5 cm²⁷.



(b) Cylindrical model with radius set to 5 cm²⁸.



(c) Anatomical model of the human ear, taken from Kapetanovic, Sacco et al. 2022²⁹.

²⁷Kapetanovic and Poljak 2022.

²⁸Kapetanovic and Poljak 2023.

²⁹Kapetanovic, Sacco, et al. 2022.

Normal estimation on canonical surfaces is straightforward

- Cartesian $(x, y, z) \rightarrow$ ISO 80000-2:2019 spherical (r, θ, φ) coordinate system:
 - r – the radial distance, i.e., the distance to origin
 - θ – the polar angle
 - φ – the angle of rotation from the initial meridian plane, i.e., azimuth angle
- the parametric representation of the spherical surface assuming constant r
- unit vector normal to the parametric surface

$$\mathbf{v}(\theta, \varphi) = [r \sin(\theta) \cos(\varphi), r \sin(\theta) \sin(\varphi), r \cos(\theta)]$$

$$\hat{\mathbf{n}} = -\frac{\mathbf{v}_\theta \times \mathbf{v}_\varphi}{|\mathbf{v}_\theta \times \mathbf{v}_\varphi|}$$

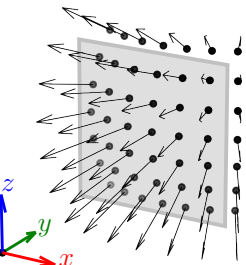


Figure: Spherical averaging area.

Normal estimation on canonical surfaces is straightforward

- Cartesian $(x, y, z) \rightarrow$ ISO 80000-2:2019 cylindrical (r, θ, z) coordinate system:
 - r – the radial distance, i.e., the distance to origin
 - φ – the angle of rotation from the initial meridian plane, i.e., azimuth angle
 - z – the axial coordinate
- the parametric representation of the cylindrical surface assuming constant r

$$\mathbf{v}(\varphi, z) = [r \cos(\varphi), r \sin(\varphi), z]$$

- unit vector normal to the parametric surface

$$\hat{\mathbf{n}} = -\frac{\mathbf{v}_\theta \times \mathbf{v}_\varphi}{|\mathbf{v}_\theta \times \mathbf{v}_\varphi|}$$

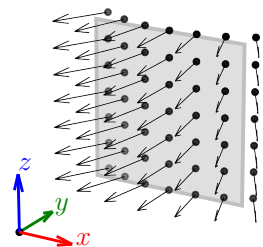


Figure: Cylindrical averaging area.

Normal vector estimation on anatomical models

- assign a normal vector, \hat{n} , at each point, x_i of the point cloud,
 $\mathbb{X} = \{x_1, x_2, \dots, x_n\} \subset \mathbb{R}^2$
- organize \mathbb{X} into k-d tree and extract k nearest neighbors of x_i , $nghd(x_i)$
- create the scatter matrix and compute its principal components
- the eigenvector with the smallest corresponding eigenvalue is orthogonal to the tangent plane $\rightarrow \hat{n}$
- eigenvectors with greater eigenvalues indicate greater variance \rightarrow unit binormal, \hat{b} , and tangent vector, \hat{t}
- repeat this for each x_i in \mathbb{X}

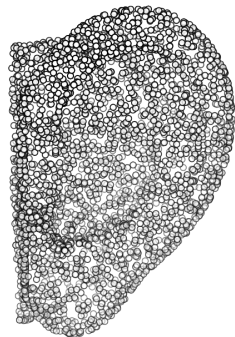


Figure: Point cloud of the anatomical tissue model.

Normal vector estimation on anatomical models

- assign a normal vector, \hat{n} , at each point, x_i of the point cloud,
 $\mathbb{X} = \{x_1, x_2, \dots, x_n\} \subset \mathbb{R}^2$
- organize \mathbb{X} into k-d tree and extract k nearest neighbors of x_i , $nghd(x_i)$
- create the scatter matrix and compute its principal components
- the eigenvector with the smallest corresponding eigenvalue is orthogonal to the tangent plane $\rightarrow \hat{n}$
- eigenvectors with greater eigenvalues indicate greater variance \rightarrow unit binormal, \hat{b} , and tangent vector, \hat{t}
- repeat this for each x_i in \mathbb{X}

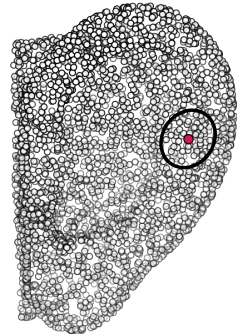


Figure: Target point x_i in its local neighborhood defined with a fixed number of neighboring points or within a predefined distance.

Normal vector estimation on anatomical models

- assign a normal vector, \hat{n} , at each point, x_i of the point cloud,
 $\mathbb{X} = \{x_1, x_2, \dots, x_n\} \subset \mathbb{R}^2$
- organize \mathbb{X} into k-d tree and extract k nearest neighbors of x_i , $nbhd(x_i)$
- create the scatter matrix and compute its principal components
- the eigenvector with the smallest corresponding eigenvalue is orthogonal to the tangent plane $\rightarrow \hat{n}$
- eigenvectors with greater eigenvalues indicate greater variance \rightarrow unit binormal, \hat{b} , and tangent vector, \hat{t}
- repeat this for each x_i in \mathbb{X}

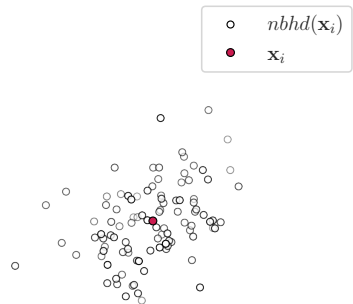


Figure: Local patch of points used for fitting the tangent plane.

Normal vector estimation on anatomical models

- assign a normal vector, \hat{n} , at each point, x_i of the point cloud,
 $\mathbb{X} = \{x_1, x_2, \dots, x_n\} \subset \mathbb{R}^2$
- organize \mathbb{X} into k-d tree and extract k nearest neighbors of x_i , $nbhd(x_i)$
- create the scatter matrix and compute its principal components
- the eigenvector with the smallest corresponding eigenvalue is orthogonal to the tangent plane $\rightarrow \hat{n}$
- eigenvectors with greater eigenvalues indicate greater variance \rightarrow unit binormal, \hat{b} , and tangent vector, \hat{t}
- repeat this for each x_i in \mathbb{X}

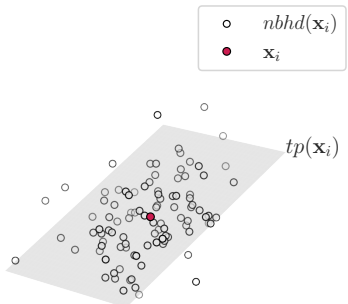


Figure: The best fitting tangent plane.

Normal vector estimation on anatomical models

- assign a normal vector, \hat{n} , at each point, x_i of the point cloud,
 $\mathbb{X} = \{x_1, x_2, \dots, x_n\} \subset \mathbb{R}^2$
- organize \mathbb{X} into k-d tree and extract k nearest neighbors of x_i , $nbhd(x_i)$
- create the scatter matrix and compute its principal components
- the eigenvector with the smallest corresponding eigenvalue is orthogonal to the tangent plane $\rightarrow \hat{n}$
- eigenvectors with greater eigenvalues indicate greater variance \rightarrow unit binormal, \hat{b} , and tangent vector, \hat{t}
- repeat this for each x_i in \mathbb{X}

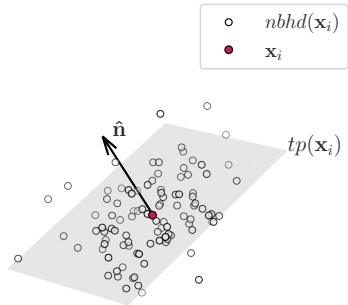


Figure: The unit normal vector in x_i is orthogonal to the local tangent plane.

Normal vector estimation on anatomical models

- assign a normal vector, \hat{n} , at each point, x_i of the point cloud,
 $\mathbb{X} = \{x_1, x_2, \dots, x_n\} \subset \mathbb{R}^2$
- organize \mathbb{X} into k-d tree and extract k nearest neighbors of x_i , $nbhd(x_i)$
- create the scatter matrix and compute its principal components
- the eigenvector with the smallest corresponding eigenvalue is orthogonal to the tangent plane $\rightarrow \hat{n}$
- eigenvectors with greater eigenvalues indicate greater variance \rightarrow unit binormal, \hat{b} , and tangent vector, \hat{t}
- repeat this for each x_i in \mathbb{X}

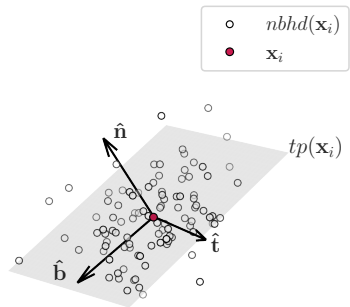


Figure: The unit binormal and tangent vector – tangential components of an orthonormal basis.

Normal vector estimation on anatomical models

- assign a normal vector, \hat{n} , at each point, x_i of the point cloud,
 $\mathbb{X} = \{x_1, x_2, \dots, x_n\} \subset \mathbb{R}^2$
- organize \mathbb{X} into k-d tree and extract k nearest neighbors of x_i , $nhd(x_i)$
- create the scatter matrix and compute its principal components
- the eigenvector with the smallest corresponding eigenvalue is orthogonal to the tangent plane $\rightarrow \hat{n}$
- eigenvectors with greater eigenvalues indicate greater variance \rightarrow unit binormal, \hat{b} , and tangent vector, \hat{t}
- repeat this for each x_i in \mathbb{X}



Figure: Distribution of the unit vector field normal to the surface.

Local tangent plane fitting

- $n\text{bhd}(\mathbf{x}_i)$ is represented with the “centroid”

$$\mathbf{m}_i = \frac{1}{k} \sum_{j=1}^k \mathbf{x}_j$$

where $\mathbf{x}_j \in n\text{bhd}(\mathbf{x}_i)$

- the tangential plane can then be found by minimizing the Euclidian vector distance, \mathbf{y}_j between each point in $n\text{bhd}(\mathbf{x}_i)$ and \mathbf{m}_i

$$\min_{|\mathbf{n}_i|=1} \sum_{j=1}^k (\mathbf{y}_j^\top \mathbf{n}_i)^2$$

- this expression can be rewritten in a matrix notation as

$$\min_{\mathbf{n}_i^\top \mathbf{n}_i = 1} \mathbf{n}_i^\top (\mathbf{Y}_i \mathbf{Y}_i^\top) \mathbf{n}_i$$

where

$$\mathbf{Y}_i = \begin{pmatrix} | & | & & | & & | \\ \mathbf{y}_1 & \mathbf{y}_2 & \cdots & \mathbf{y}_j & \cdots & \mathbf{y}_k \\ | & | & & | & & | \end{pmatrix}$$

Constrained minimization via Lagrange multipliers

- a function $f(\mathbf{n}_i) = \mathbf{n}_i^\top \mathbf{S}_i \mathbf{n}_i$ where $\mathbf{S}_i = \mathbf{Y}_i \mathbf{Y}_i^\top$ should be minimized s.t.
 $\mathbf{n}_i^\top \mathbf{n}_i = 1$
- instead of constrained optimization, $f(\mathbf{n}_i)$ is subjected to the equality constraint
 $g(\mathbf{n}_i) = \mathbf{n}_i^\top \mathbf{n}_i - 1$ and the Lagrangian function is formed

$$\mathcal{L}(\mathbf{n}_i, \lambda) = f(\mathbf{n}_i) - \lambda g(\mathbf{n}_i)$$

- the constrained minimization of $f(\mathbf{n}_i)$ is now equivalent to the unconstrained minimization of $\mathcal{L}(\mathbf{n}_i, \lambda)$

$$\nabla \mathcal{L}(\mathbf{n}_i, \lambda) = 0$$

$$\frac{\partial \mathcal{L}}{\partial \mathbf{n}_i} = 0 \Rightarrow \mathbf{S}_i \mathbf{n}_i = \lambda \mathbf{n}_i$$

$$\frac{\partial \mathcal{L}}{\partial \lambda} = 0 \Rightarrow \mathbf{n}_i^\top \mathbf{n}_i = 1$$

- the normal is the eigenvector \mathbf{S}_i with the smallest associated λ

$$\mathbf{S}_i = \mathbf{V} \begin{pmatrix} \lambda_1 & & \\ & \ddots & \\ & & \lambda_d \end{pmatrix} \mathbf{V}^\top$$

Assessment of the curvature, i.e., “non-unit” normal vector

- using the local frame computed at x_i with the principal component analysis (PCA), the placement of $nbhd(x_i)$ can be represented as $[u, v, f(u, v)]$
- the parametric surface is expressed in the local frame’s basis, i.e., with the principal component vectors
 - u, v – tangential coordinates
 - $f(u, v)$ – the “height” function in the normal direction
- instead of a plane, a higher-order polynomial³⁰, implicit B-spline³¹, n-jet (truncated Taylor expansion)³², etc. can be fitted to such parametric surface representation
- curvature normal is then computed as

$$\mathbf{n} = \frac{\partial \tilde{f}}{\partial u} \times \frac{\partial \tilde{f}}{\partial v}$$

at $u = v = 0$ where $\tilde{f}(u, v)$ is the fitted “height” function

³⁰Levin 1998.

³¹Mohammad Rouhani 2015.

³²Cazals and Pouget 2005.

Surface normal vector estimation via moving least squares

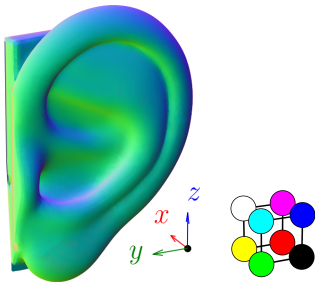


Figure: Surface normal vector field distribution estimated by moving least squares (weighted with radial basis function) applied to the parametric surface embedded in the local frame's basis.

- weighted moving least squares generally performs well and is able to capture curvature better compared to the simple plane fitting
- fails at sharp edges or corners, i.e., non-differentiable and non-smooth regions of the surface
- these issues can be alleviated by using either regression-based deep learning methods³³ or surface fitting-based deep learning methods (traditional surface fitting methods extended with the optimal set of weights)³⁴

³³Ben-Shabat, Lindenbaum, and Fischer 2019; Charles et al. 2017; Guerrero et al. 2018.

³⁴Ben-Shabat and Gould 2020; Lenssen, Osendorfer, and Masci 2020; Zhu et al. 2021.

Surface normal vector estimation via moving least squares

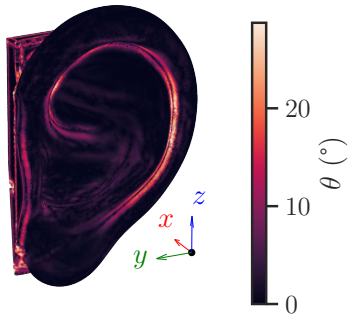


Figure: Spatial distribution of angle error between normals computed by using moving least squares and PCA (ground truth, but still prone to instabilities and errors).

- weighted moving least squares generally performs well and is able to capture curvature better compared to the simple plane fitting
- fails at sharp edges or corners, i.e., non-differentiable and non-smooth regions of the surface
- these issues can be alleviated by using either regression-based deep learning methods³³ or surface fitting-based deep learning methods (traditional surface fitting methods extended with the optimal set of weights)³⁴

³³Ben-Shabat, Lindenbaum, and Fischer 2019; Charles et al. 2017; Guerrero et al. 2018.

³⁴Ben-Shabat and Gould 2020; Lenssen, Osendorfer, and Masci 2020; Zhu et al. 2021.

Surface normal vector estimation via moving least squares

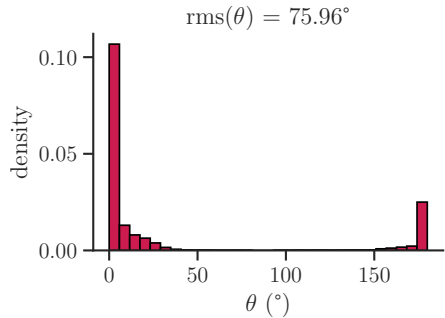


Figure: Histogram of angle error – difficulty in dealing with non-differentiable regions results in large deviations.

- weighted moving least squares generally performs well and is able to capture curvature better compared to the simple plane fitting
- fails at sharp edges or corners, i.e., non-differentiable and non-smooth regions of the surface
- these issues can be alleviated by using either regression-based deep learning methods³³ or surface fitting-based deep learning methods (traditional surface fitting methods extended with the optimal set of weights)³⁴

³³Ben-Shabat, Lindenbaum, and Fischer 2019; Charles et al. 2017; Guerrero et al. 2018.

³⁴Ben-Shabat and Gould 2020; Lenssen, Osendorfer, and Masci 2020; Zhu et al. 2021.

Normal orientation

- the local frame at x_i contains arbitrarily oriented eigenvectors due to PCA
- consistent orientation – normals, \mathbf{n}_i and \mathbf{n}_j , of any two neighboring points, x_i and x_j , should point in similar direction
- $\mathbf{n}_i \cdot \mathbf{n}_j \approx \pm 1 \rightarrow tp(x_i)$ and $tp(x_j)$ are parallel
- $\mathbf{n}_i \cdot \mathbf{n}_j \approx 1 \checkmark$
- if above condition is not met, \mathbf{n}_i or \mathbf{n}_j should be flipped
- disadvantages:
 - ① fails at sharp edges and corners
 - ② the condition should hold for *all* pairs of neighboring points in the point cloud

Normal orientation

- the local frame at x_i contains arbitrarily oriented eigenvectors due to PCA
 - consistent orientation – normals, \mathbf{n}_i and \mathbf{n}_j , of any two neighboring points, x_i and x_j , should point in similar direction
 - $\mathbf{n}_i \cdot \mathbf{n}_j \approx \pm 1 \rightarrow tp(x_i)$ and $tp(x_j)$ are parallel
 - $\mathbf{n}_i \cdot \mathbf{n}_j \approx 1 \checkmark$
 - if above condition is not met, \mathbf{n}_i or \mathbf{n}_j should be flipped
 - disadvantages possible solutions:
 - ① anatomical tissue models do not contain sharp edges and corners; otherwise methods that handle noise, outliers and sharp features available³⁵
 - ② posing a problem as graph optimization by:
 - constructing a graph over the point cloud
 - applying a weight to each edge based on the similarity score between the respective points' normals
- $$w_{ij} = 1 - |\mathbf{n}_i \cdot \mathbf{n}_j|$$
- constructing a minimal spanning tree
 - propagating the normal orientation from a single point selected as the root
 - the favorable propagation along directions of low curvature \rightarrow avoiding edges

³⁵Huang et al. 2009.

Surface integration on arbitrary-shaped evaluation surface

- for the surface-normal propagation-direction power density into the evaluation surface, the spatial average should be computed according to

$$S = \frac{1}{2A_{av}} \iint_A \Re[\mathbf{E} \times \mathbf{H}^*] \cdot \hat{\mathbf{n}} \Theta\left\{ \Re[\mathbf{E} \times \mathbf{H}^*] \cdot \hat{\mathbf{n}} \right\} dA_{av}$$

where

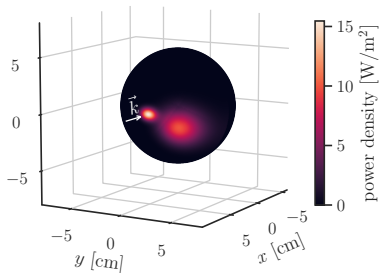
- $\Theta(\cdot)$ – the Heaviside (unit step) function
- A_{av} – non-planar evaluation surface
- contributions from regions where the Poynting vector is oriented outward from or is close to parallel to the evaluation surface will not be considered as the Heaviside function will be ~ 0
- $A_{av} > A$
 - the more pronounced the curvature, the greater the difference
 - A_{av} can be estimated directly by integrating the normals
- numerical integration – the 2-D adaptive Gauss–Kronrod quadrature formula as implemented in QUADPACK

Automatic detection of the “hot-spot” region

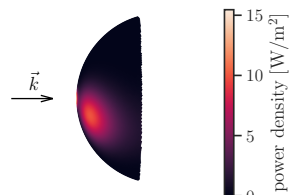
- ① assuming that a non-planar model is given as the oriented set of points $\mathbb{X} = \{\mathbf{x}_1, \mathbf{x}_2, \dots, \mathbf{x}_n\} \subset \mathbb{R}^3$, organize it in a 3-D k-d tree
- ② extract only the points visible from the predefined direction³⁶, i.e., the EM field propagation direction – only directly irradiated regions investigated
- ③ for each point in the visible subset of points, extract the local neighborhood of points placed within a sphere of a radius $r_c = \sqrt{2A}$ where A is the planar averaging area
- ④ change of basis of the local neighborhood by using PCA and extract the subset of points that placed within a square-shaped region of area A , aligned to correspond to tangential principal components
- ⑤ compute the area of a non-planar evaluation surface, A_{av} , by approximating surface integral of normals on this surface
- ⑥ perform double quadrature of the power density on this surface and extract the spatially averaged value

³⁶Katz, Tal, and Basri 2007.

“Hot-spot” detection algorithm in action algorithm



(a) Exposure scenario in 3-D point of view.



(b) 3-D point cloud after removing the hidden points from the direction of incidence point of view.

Figure: Click [here](#) to make me dance!

Table of contents

1. Introduction
2. Materials and methods
3. Applications and experimental results
4. Concluding remarks

Applications and experimental results

- Kapetanovic, A. and Poljak, D. “Assessment of incident power density on spherical head model up to 100 GHz,” in *IEEE Trans Electromagn Compat*, 64(5):1296–1303
- Kapetanovic, A., Susnjara, A., et al. “Stochastic-deterministic electromagnetic modeling of human head exposure to Microsoft HoloLens,” proceedings of 2022 *International Conference on Software, Telecommunications and Computer Networks (SoftCOM)*, Split, Croatia
- Kapetanovic, A. and Poljak, D. “Machine learning-assisted antenna modeling for realistic assessment of incident power density on non-planar surfaces above 6 GHz,” in *Radiat Prot Dosim*, pending publication, 2023
- Kapetanovic, A. Sacco, G., et al. “Assessment of area-average absorbed power density on realistic tissue models at mmWaves,” proceedings of 2022 *IEEE MTT-S International Microwave Biomedical Conference (IMBioC)*, Suzhou, China
- Kapetanovic, A. Sacco, G., et al. “Area-averaged transmitted and absorbed power density on a realistic ear model,” in *IEEE J Electromagn RF Microw Med Biol*, 7(1)39–45, 2023

Applications and experimental results

- Kapetanovic, A. and Poljak, D. “Assessment of incident power density on spherical head model up to 100 GHz,” in *IEEE Trans Electromagn Compat*, 64(5):1296–1303

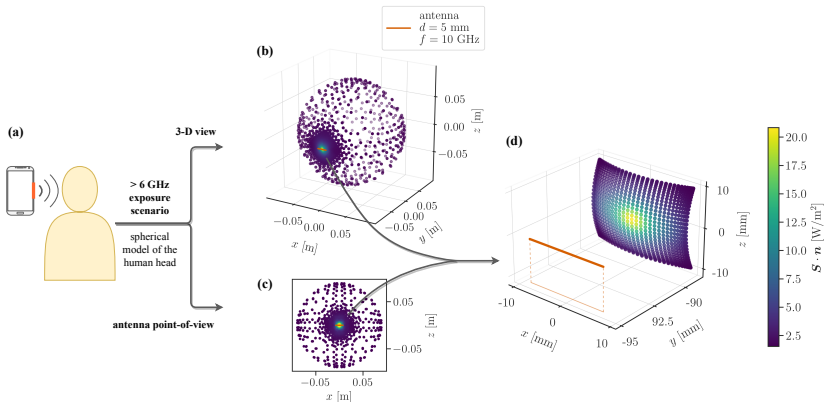


Figure: Overview of the exposure scenario.

Applications and experimental results

- Kapetanovic, A. and Poljak, D. “Assessment of incident power density on spherical head model up to 100 GHz,” in *IEEE Trans Electromagn Compat*, 64(5):1296–1303
 - assessment of the spatially averaged IPD on a spherical human head model at 3.5–100 GHz
 - the spatially-averaged IPD defined either by averaging components of the power density vector normal to an valuation surface, or by averaging its norm
 - EM source – a dipole antenna placed at a separation distance 2–150 mm from the curved model and compared with differently positioned planar surfaces
 - appropriate settings of exposure – IPD up to 12 % greater for the surface-normal propagation-direction
 - the worst case scenario – IPD up to 30 % larger regardless of definition
 - reactive near-field conditions – norm definition of IPD > normal defintion of IPD

Applications and experimental results

- Kapetanovic, A., Susnjara, A., et al. "Stochastic-deterministic electromagnetic modeling of human head exposure to Microsoft HoloLens," proceedings of 2022 *International Conference on Software, Telecommunications and Computer Networks (SoftCOM)*, Split, Croatia

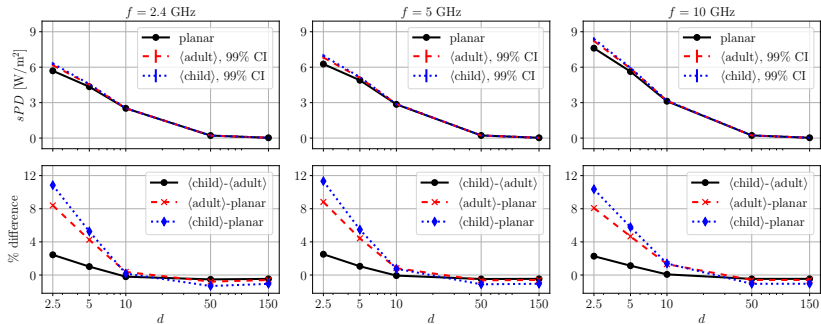


Figure: IPD averaged on the adult and child head as a function of the separation distance at different frequencies compared to a reference flat evaluation surface.

Applications and experimental results

- Kapetanovic, A., Susnjara, A., et al. “Stochastic-deterministic electromagnetic modeling of human head exposure to Microsoft HoloLens,” proceedings of 2022 *International Conference on Software, Telecommunications and Computer Networks (SoftCOM)*, Split, Croatia
 - assessment of the spatially averaged IPD on a spherical human head model at 2.4 GHz, 5 GHz and 10 GHz
 - the effect of the curvature of the average adult and child head on spatially averaged IPD
 - stochastic analysis indicate marginal difference between models
 - comparative analysis of the spatially averaged IPD on highly curved and almost flat body parts – relative differences of up to 20 %
 - spherical head models yield significantly higher values of the spatially averaged IPD (up to 25 %) compared to standard planar tissue models

Applications and experimental results

- Kapetanovic, A. and Poljak, D. “Machine learning-assisted antenna modeling for realistic assessment of incident power density on non-planar surfaces above 6 GHz,” in *Radiat Prot Dosim*, pending publication, 2023

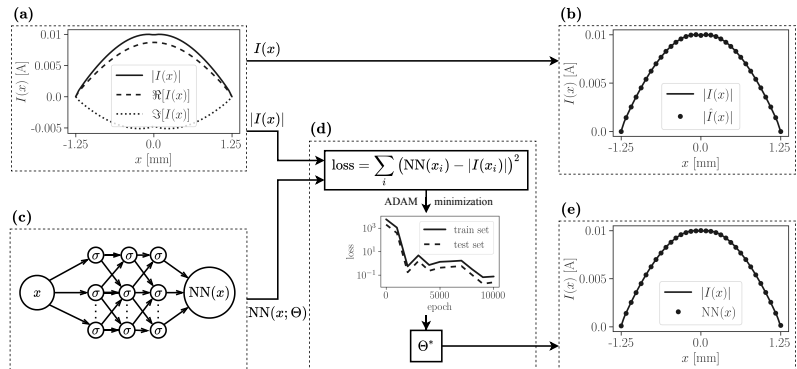


Figure: Machine learning-assisted antenna modeling workflow overview.

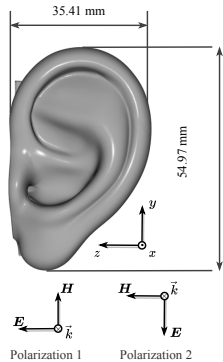
Applications and experimental results

- Kapetanovic, A. and Poljak, D. “Machine learning-assisted antenna modeling for realistic assessment of incident power density on non-planar surfaces above 6 GHz,” in *Radiat Prot Dosim*, pending publication, 2023
 - IPD spatially averaged over the spherical and cylindrical surface computed at 6–90 GHz
 - high frequencies → numerical artifacts during computational EM modeling
 - machine learning and its associated tooling (automatic differentiation) + traditional scientific computing = differentiable programming → elimination of numerical artifacts and computational speed-up
 - curvature of non-planar models – strong positive association with larger values of spatially averaged IPD

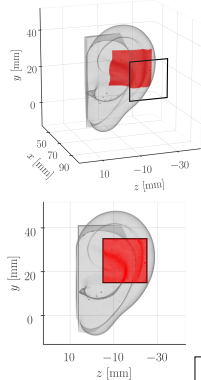
Applications and experimental results

- Kapetanovic, A. Sacco, G., et al. “Area-averaged transmitted and absorbed power density on a realistic ear model,” in *IEEE J Electromagn RF Microw Med Biol*, 7(1)39–45, 2023

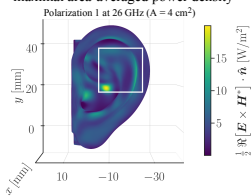
A CAD EM model of an adult ear



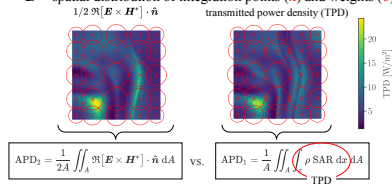
B projection of the integration domain



C maximal area-averaged power density



D spatial distribution of integration points (**x**) and weights (**o**)



Applications and experimental results

- Kapetanovic, A. Sacco, G., et al. “Area-averaged transmitted and absorbed power density on a realistic ear model,” in *IEEE J Electromagn RF Microw Med Biol*, 7(1)39–45, 2023
 - extension of Kapetanovic, A. Sacco, G., et al. “Assessment of area-average absorbed power density on realistic tissue models at mmWaves,” proceedings of *2022 IEEE MTT-S International Microwave Biomedical Conference (IMBioC)*, Suzhou, China – the best student paper award!
 - a new iterative technique for accurate evaluation of the APD on an evaluation surface of arbitrary geometry
 - analysis of the plane wave exposure at 26 GHz and 60 GHz
 - two definitions of APD compared – the relative difference within 6 %
 - APD on anatomical model up to 20 % greater compared to flat tissue models

Table of contents

1. Introduction
2. Materials and methods
3. Applications and experimental results
4. Concluding remarks

Main contributions

- more realistic (non-planar canonical or anatomical) models of human body parts exposed to RF EM fields above 6 GHz, replacing previous flat models
- the accurate numerical technique for efficiently evaluating the scalar and vector field surface integrals
- the computationally efficient algorithm for automatic detection of “hot-spots” regions is developed for proposed models
- extensive dosimetric analysis of absorbed and incident EM power density using rigorous mathematical definitions and without simplification of the evaluation surface morphology

Additional contributions

- confirmation of the validity of APD as BR for maximum superficial temperature rise during local exposure of curved body parts above 6 GHz in steady state
- insights into the efficiency of non-planar canonical and anatomical models for EM dosimetry at RF, providing a foundation for future discussions and activities of working group 7 under IEEE/ICES TC 95 SC 6 for EM dosimetry modeling
- a basis for discussions on the implementation of non-planar models as reference for future generations of ICNIRP guidelines and IEEE standards

Questions and answers

Thank you!

References I

-  Anderson, V., R. Croft, and R. L. McIntosh (2010). “SAR versus S_{inc} : What is the appropriate RF exposure metric in the range 1–10 GHz? Part I: Using planar body models”. In: *Bioelectromagnetics* 31.6, pp. 454–466. DOI: [10.1002/bem.20578](https://doi.org/10.1002/bem.20578).
-  Andrews, J. G. et al. (2014). “What will 5G be?” In: *IEEE Journal on Selected Areas in Communications* 32.6, pp. 1065–1082. DOI: [10.1109/JSAC.2014.2328098](https://doi.org/10.1109/JSAC.2014.2328098).
-  Ben-Shabat, Y. and Stephen Gould (2020). “DeepFit: 3D surface fitting via neural network weighted least squares”. In: *arXiv preprint arXiv:2003.10826*.
-  Ben-Shabat, Y., M. Lindenbaum, and A. Fischer (2019). “Nesti-Net: Normal estimation for unstructured 3D point clouds Using convolutional neural networks”. In: *2019 IEEE/CVF Conference on Computer Vision and Pattern Recognition (CVPR)*, pp. 10104–10112. DOI: [10.1109/CVPR.2019.01035](https://doi.org/10.1109/CVPR.2019.01035).
-  Carrasco, E. et al. (2019). “Exposure assessment of portable wireless devices above 6 GHz”. In: *Radiation Protection Dosimetry* 183.4, pp. 489–496. DOI: [10.1093/rpd/ncy177](https://doi.org/10.1093/rpd/ncy177).

References II

-  Cazals, F. and M. Pouget (2005). "Estimating differential quantities using polynomial fitting of osculating jets". In: *Computer Aided Geometric Design* 22.2, pp. 121–146. DOI: [10.1016/j.cagd.2004.09.004](https://doi.org/10.1016/j.cagd.2004.09.004).
-  Charles, R. Q. et al. (2017). "PointNet: Deep learning on point sets for 3D classification and segmentation". In: *2017 IEEE Conference on Computer Vision and Pattern Recognition (CVPR)*, pp. 77–85. DOI: [10.1109/CVPR.2017.16](https://doi.org/10.1109/CVPR.2017.16).
-  Colombi, D., B. Thors, and C. Törnevik (2015). "Implications of EMF exposure limits on output power levels for 5G devices above 6 GHz". In: *IEEE Antennas and Wireless Propagation Letters* 14, pp. 1247–1249. DOI: [10.1109/LAWP.2015.2400331](https://doi.org/10.1109/LAWP.2015.2400331).
-  De Santis, V. et al. (2022). "On the correlation between incident power density and temperature increase for exposures at frequencies above 6 GHz". In: *IEEE Access* 10, pp. 82236–82245. DOI: [10.1109/ACCESS.2022.3195887](https://doi.org/10.1109/ACCESS.2022.3195887).
-  Diao, Y., K. Li, et al. (2021). "Effect of incidence angle on the spatial-average of incident power density definition to correlate skin temperature rise for millimeter wave exposures". In: *IEEE Transactions on Electromagnetic Compatibility* 63.5, pp. 1709–1716. DOI: [10.1109/TEMC.2021.3098594](https://doi.org/10.1109/TEMC.2021.3098594).

References III

-  Diao, Y., E. Rashed, and A. Hirata (2020). "Assessment of absorbed power density and temperature rise for non-planar body model under electromagnetic exposure above 6 GHz". In: *Physics in medicine & biology* 65.22, p. 224001. DOI: [10.1088/1361-6560/abbdb7](https://doi.org/10.1088/1361-6560/abbdb7).
-  Foster, K. R., M. C. Ziskin, and Q. Balzano (2016). "Thermal response of human skin to microwave energy: a critical review". In: *Health Physics* 111.6, pp. 528–541. DOI: [10.1097/HP.0000000000000571](https://doi.org/10.1097/HP.0000000000000571).
-  — (2017). "Thermal Modeling for the Next Generation of Radio-frequency Exposure Limits: Commentary". In: *Health physics* 113.1, pp. 41–53. DOI: [10.1097/HP.0000000000000671](https://doi.org/10.1097/HP.0000000000000671).
-  Foster, K. R., M. C. Ziskin, Q. Balzano, and G. Bit-Babik (2018). "Modeling tissue heating from exposure to radio-frequency energy and relevance of tissue heating to exposure limits: Heating factor". In: *Health Physics* 115.2, pp. 295–307. DOI: [10.1097/HP.0000000000000854](https://doi.org/10.1097/HP.0000000000000854).
-  Funahashi, D., A. Hirata, et al. (2018). "Area-averaged transmitted power density at skin surface as metric to estimate surface temperature elevation". In: *IEEE Access* 6, pp. 77665–77674. DOI: [10.1109/ACCESS.2018.2883733](https://doi.org/10.1109/ACCESS.2018.2883733).

References IV

-  Funahashi, D., T. Ito, et al. (2018). "Averaging area of incident power density for human exposure from patch antenna arrays". In: *IEICE Transactions on Electronics* E101.C.8, pp. 644–646. DOI: [10.1587/transele.E101.C.644](https://doi.org/10.1587/transele.E101.C.644).
-  Gabriel, C. (1996). "Compilation of the dielectric properties of body tissues at RF and microwave frequencies". In: *US Air Force*. Vol. Final Technical Report, TR-1996-0037. DOI: [10.21236/ada303903](https://doi.org/10.21236/ada303903).
-  Guerrero, P. et al. (2018). "PCPNet: Learning local shape properties from raw point clouds". In: *Computer Graphics Forum* 37.2, pp. 75–85. DOI: [10.1111/cgf.13343](https://doi.org/10.1111/cgf.13343).
-  Hashimoto, Y. et al. (2017). "On the averaging area for incident power density for human exposure limits at frequencies over 6 GHz". In: *Physics in Medicine & Biology* 62.8, pp. 3124–3138. DOI: [10.1088/1361-6560/aa5f21](https://doi.org/10.1088/1361-6560/aa5f21).
-  He, W. et al. (2018). "RF compliance study of temperature elevation in human head model around 28 GHz for 5G user equipment application: Simulation analysis". In: *IEEE Access* 6, pp. 830–838. DOI: [10.1109/ACCESS.2017.2776145](https://doi.org/10.1109/ACCESS.2017.2776145).

References V

-  Huang, H. et al. (2009). "Consolidation of unorganized point clouds for surface reconstruction". In: *ACM Transactions on Graphics* 28.5, pp. 1–7. DOI: [10.1145/1618452.1618522](https://doi.org/10.1145/1618452.1618522).
-  IEEE International Committee on Electromagnetic Safety (ICES) Technical Committee (TC) 95 (2019). "Standard for safety levels with respect to human exposure to electric, magnetic, and electromagnetic fields, 0 Hz to 300 GHz". In: *IEEE Std C95.1-2019 (Revision of IEEE Std C95.1-2005/ Incorporates IEEE Std C95.1-2019/Cor 1-2019)*, pp. 1–312. DOI: [10.1109/IEEESTD.2019.8859679](https://doi.org/10.1109/IEEESTD.2019.8859679).
-  — (2021). "Guide for the definition of incident power density to correlate surface temperature elevation". In: *IEEE Std 2889-2021*, pp. 1–152. DOI: [10.1109/IEEESTD.2021.9650810](https://doi.org/10.1109/IEEESTD.2021.9650810).
-  International Commission on Non-Ionizing Radiation Protection (ICNIRP) (2020a). "Guidelines for limiting exposure to electromagnetic fields (100 kHz to 300 GHz)". In: *Health Physics* 118, pp. 483–524. DOI: [10.1097/HP.0000000000001210](https://doi.org/10.1097/HP.0000000000001210).
-  — (2020b). "Principles for non-ionizing radiation protection". In: *Health Physics* 118.5, pp. 477–482. DOI: [10.1097/HP.0000000000001252](https://doi.org/10.1097/HP.0000000000001252).

References VI

-  Kapetanovic, A. and D. Poljak (2022). "Assessment of incident power density on spherical head model up to 100 GHz". In: *IEEE Transactions on Electromagnetic Compatibility* 64.5, pp. 1296–1303. DOI: 10.1109/TEMC.2022.3183071.
-  — (2023). "Machine learning-assisted antenna modelling for realistic assessment of incident power density on non-planar surfaces above 6 GHz". In: *Radiation Protection Dosimetry* pending publication, pp. 1–9. DOI: 10.1093/rpd/ncad114.
-  Kapetanovic, A., G. Sacco, et al. (2022). "Area-averaged transmitted and absorbed power density on a realistic ear model". In: *IEEE Journal of Electromagnetics, RF and Microwaves in Medicine and Biology* 7.1, pp. 39–45. DOI: 10.1109/JERM.2022.3225380.
-  Katz, S., A. Tal, and R. Basri (2007). "Direct visibility of point sets". In: *ACM Transactions on Graphics* 26.3, pp. 24–35. DOI: 10.1145/1276377.1276407.
-  Lenssen, J. E., C. Osendorfer, and J. Masci (2020). "Deep iterative surface normal estimation". In: *2020 IEEE/CVF Conference on Computer Vision and Pattern Recognition (CVPR)*, pp. 11244–11253. DOI: 10.1109/CVPR42600.2020.01126.

References VII

-  Levin, D. (1998). "The approximation power of moving least-squares". In: *Mathematics of Computation* 67, pp. 1517–1531. DOI: [10.1090/S0025-5718-98-00974-0](https://doi.org/10.1090/S0025-5718-98-00974-0).
-  Li, C-H. et al. (2012). "Mechanisms of RF electromagnetic field absorption in human hands and fingers". In: *IEEE Transactions on Microwave Theory and Techniques* 60.7, pp. 2267–2276. DOI: [10.1109/TMTT.2012.2197019](https://doi.org/10.1109/TMTT.2012.2197019).
-  Li, K., S. Kodera, et al. (2023). "Calculated epithelial/absorbed power density for exposure from antennas at 10–90 GHz: Intercomparison study using a planar skin model". In: *IEEE Access* 11, pp. 7420–7435. DOI: [10.1109/ACCESS.2023.3238582](https://doi.org/10.1109/ACCESS.2023.3238582).
-  Li, K., K. Sasaki, K. Wake, et al. (2021). "Quantitative comparison of power densities related to electromagnetic near-field exposures with safety guidelines from 6 to 100 GHz". In: *IEEE Access* 9, pp. 115801–115812. DOI: [10.1109/ACCESS.2021.3105608](https://doi.org/10.1109/ACCESS.2021.3105608).

References VIII

-  Li, K., K. Sasaki, S. Watanabe, et al. (2019). "Relationship between power density and surface temperature elevation for human skin exposure to electromagnetic waves with oblique incidence angle from 6 GHz to 1 THz". In: *Physics in Medicine & Biology* 64.6, p. 065016. DOI: 10.1088/1361-6560/ab057a.
-  McIntosh, R. L. and V. Anderson (2010). "SAR versus S_{inc} : What is the appropriate RF exposure metric in the range 1–10 GHz? Part II: Using complex human body models". In: *Bioelectromagnetics* 31.6, pp. 467–478. DOI: 10.1002/bem.20574.
-  Miura, N. et al. (2021). "Power absorption and skin temperature rise from simultaneous near-field exposure at 2 and 28 GHz". In: *IEEE Access* 9, pp. 152140–152149. DOI: 10.1109/ACCESS.2021.3126372.
-  Mohammad Rouhani Angel D. Sappa, Edmond Boyer (2015). "Implicit B-Spline Surface Reconstruction". In: *IEEE Transactions on Image Processing* 24.1, pp. 22–32. DOI: 10.1109/TIP.2014.2366374.

References IX

-  Morimoto, R. and A. Hirata (2022). "Assessment of incident power density in different shapes of averaging area for radio-frequency exposure above 6 GHz". In: *Physics in Medicine & Biology* 67.21, p. 215014. DOI: 10.1088/1361-6560/ac994d.
-  Nakae, T. et al. (2020). "Skin temperature elevation for incident power densities from dipole arrays at 28 GHz". In: *IEEE Access* 8, pp. 26863–26871. DOI: 10.1109/ACCESS.2020.2970219.
-  Rappaport, T. S. et al. (2013). "Millimeter wave mobile communications for 5G cellular: It will work!" In: *IEEE Access* 1, pp. 335–349. DOI: 10.1109/ACCESS.2013.2260813.
-  Sacco, G., Z. Haider, and M. Zhadobov (2022). "Exposure levels induced in curved body parts at mmWaves". In: *IEEE Journal of Electromagnetics, RF and Microwaves in Medicine and Biology* 6.3, pp. 413–419. DOI: 10.1109/JERM.2022.3178604.
-  Sasaki, K. et al. (2017). "Monte Carlo simulations of skin exposure to electromagnetic field from 10 GHz to 1 THz". In: *Physics in medicine & biology* 62 (17), pp. 6993–7010. DOI: 10.1088/1361-6560/aa81fc.

References X

-  Taguchi, K. et al. (2022). "Computation of absorbed power densities in high-resolution head models by considering skin thickness in quasi-millimeter and millimeter wave bands". In: *IEEE Journal of Electromagnetics, RF and Microwaves in Medicine and Biology* 6.4, pp. 516–523. DOI: 10.1109/JERM.2022.3203576.
-  Thors, B. et al. (2016). "Exposure to RF EMF from array antennas in 5G mobile communication equipment". In: *IEEE Access* 4, pp. 7469–7478. DOI: 10.1109/ACCESS.2016.2601145.
-  World Health Organization (WHO) (2022). *Constitution of the World Health Organization – Preamble*. URL: <https://www.who.int/about/governance/constitution> (visited on 12/14/2022).
-  Wu, T., T. S. Rappaport, and C. M. Collins (2015). "Safe for generations to come: Considerations of safety for millimeter waves in wireless communications". In: *IEEE Microwave Magazine* 16.2, pp. 65–84. DOI: 10.1109/MMM.2014.2377587.

References XI

-  Xu, B. et al. (2017). "Understandings of maximum spatially-averaged power density in 5G RF EMF exposure study". In: *2017 International Workshop on Antenna Technology: Small Antennas, Innovative Structures, and Applications (iWAT)*, pp. 115–117. DOI: [10.1109/IWAT.2017.7915332](https://doi.org/10.1109/IWAT.2017.7915332).
-  Zhadobov, M. et al. (2011). "Millimeter-wave interactions with the human body: state of knowledge and recent advances". In: *International Journal of Microwave and Wireless Technologies* 3.2, pp. 237–247. DOI: [10.1017/S1759078711000122](https://doi.org/10.1017/S1759078711000122).
-  Zhu, R. et al. (2021). "AdaFit: Rethinking learning-based normal estimation on point clouds". In: *2021 IEEE/CVF International Conference on Computer Vision (ICCV)*, pp. 6098–6107. DOI: [10.1109/ICCV48922.2021.00606](https://doi.org/10.1109/ICCV48922.2021.00606).
-  Ziskin, M. C. et al. (2018). "Tissue models for RF exposure evaluation at frequencies above 6 GHz". In: *Bioelectromagnetics* 39.3, pp. 173–189. DOI: [10.1002/bem.22110](https://doi.org/10.1002/bem.22110).